

In-situ TEM investigation of nano-scale helium bubble evolution in tantalum-doped tungsten at 800 °C

Ipatova, Iuliia; Greaves, Graeme; Pacheco-Gutiérrez, Salvador; Middleburgh, Simon; Rushton, Michael; Jimenez-Melero, Enrique

Journal of Nuclear Materials

DOI:

[10.1016/j.jnucmat.2021.152910](https://doi.org/10.1016/j.jnucmat.2021.152910)

Published: 01/07/2021

Peer reviewed version

[Cyswllt i'r cyhoeddiad / Link to publication](#)

Dyfyniad o'r fersiwn a gyhoeddwyd / Citation for published version (APA):

Ipatova, I., Greaves, G., Pacheco-Gutiérrez, S., Middleburgh, S., Rushton, M., & Jimenez-Melero, E. (2021). In-situ TEM investigation of nano-scale helium bubble evolution in tantalum-doped tungsten at 800 °C. *Journal of Nuclear Materials*, 550, Article 152910.
<https://doi.org/10.1016/j.jnucmat.2021.152910>

Hawliau Cyffredinol / General rights

Copyright and moral rights for the publications made accessible in the public portal are retained by the authors and/or other copyright owners and it is a condition of accessing publications that users recognise and abide by the legal requirements associated with these rights.

- Users may download and print one copy of any publication from the public portal for the purpose of private study or research.
- You may not further distribute the material or use it for any profit-making activity or commercial gain
- You may freely distribute the URL identifying the publication in the public portal ?

Take down policy

If you believe that this document breaches copyright please contact us providing details, and we will remove access to the work immediately and investigate your claim.

In-situ TEM investigation of nano-scale helium bubble evolution in tantalum-doped tungsten at 800 °C

I. Ipatova^{a*}, G. Greaves^b, S. Pacheco-Gutiérrez^c, S.C. Middleburgh^a, M.J.D. Rushton^a,

E. Jimenez-Melero^d

^aNuclear Futures institute, Bangor University, Dean Street,

Bangor Gwynedd, LL57 1 UT, UK

^bSchool of Computing and Engineering, University of Huddersfield,

Huddersfield, HD1 3DH, UK

^c UKAEA - RACE, Culham Science Centre, Abingdon, OX14 3DB, UK

^dMaterials Performance Centre, Department of Materials, The University of Manchester,

Manchester M13 9PL, UK

Corresponding author (*):

Nuclear Futures Institute

Bangor University

Dean Street

Bangor Gwynedd

LL57 1UT

United Kingdom

Tel.: +44 7849290480

Email: i.ipatova@bangor.ac.uk

Abstract

The aim of this work is to probe the helium induced defect production and accumulation in 40 keV He⁺ irradiated polycrystalline W and its alternative alloy W-5wt.%Ta using transmission electron microscopy (TEM) combined with in-situ helium irradiation at 800°C. A maximum damage level of 1 dpa with a maximum He-to-dpa ratio of 5.5 at%/dpa has been reached in this work for both materials, which corresponds to an ion fluence of 7.33×10^{16} He⁺/cm². The presence of radiation-induced dislocation loops was not observed at this temperature. The low density of the incipient bubbles in W has been already detected at 0.004 dpa, which corresponds to a fluence of 3.3×10^{14} He⁺/cm². The experiments conducted at 800 °C have shown that the addition of 5wt.% of tantalum into tungsten may diminish the binding of He ions with vacancies into complexes, which serve as the core of the bubble, thus hindering helium bubble formation below 0.02 dpa and their further growth and population at higher damage levels. By exceeding the damage dose ≥ 0.3 dpa, a progressive transition from a spherical to a faceted shape of the bubbles has been observed in W but not in the W-5Ta alloy. At 1 dpa, >80% of the bubbles in W were of the faceted type with the facet planes of {110}.

Keywords: W/W-5Ta; fusion materials; in-situ helium exposure; faceted helium defects; transmission electron microscopy; bubble detection.

Introduction

Tungsten and its engineered alloys are the preferred choice as armour material for plasma-facing components (PFCs) by the nuclear fusion community, and therefore lie at the heart of the international roadmap for the realisation and deployment of fusion reactor technology [1, 2]. In ITER, the divertor design includes W monoblocks in the inner and outer vertical targets in each water-cooled cassette assembly [3]. The divertor itself is intended to serve as the plasma power exhaust, particle control (deuterium/tritium (DT) and He repumping), also functioning as a screen for impurities, reducing contamination [4]. The peak power flux density values for the ITER design range from 8 MW m^{-2} at most in the non-nuclear phases (H/He discharges) to 10 MWm^{-2} in the nuclear phases (DT burning discharges), corresponding to W surface temperatures of $\sim 800^\circ\text{C}$ and $\sim 1100^\circ\text{C}$ respectively [5]. This may increase to as much as 20 MWm^{-2} during transient events at the monoblock surface [6]. Radiation-induced damage levels in ITER divertor monoblocks are predicted to be ~ 0.1 dpa after a four-year ITER nuclear operation phase, prior to cassette replacement of the first divertor, and ~ 0.5 dpa for permanent divertor components during ITER's end-of-life operation [6].

An ITER-like divertor design for the future fusion demonstration power plant (DEMO) is being considered [7], alongside alternative configurations able to handle the more demanding radiation environment in the inner target of the divertor [8]. Besides this, DEMO is envisaged to comprise a first wall with a W armour joint to a reduced-activation ferritic/martensitic (RAFM) steel [9, 10], with predicted surface heat fluxes of $0.5\text{-}1.2 \text{ MWm}^{-2}$ [10, 11]. The expected lowest shield temperatures for W armour materials range from $\sim 500^\circ\text{C}$ in the first wall up to $>800\text{-}900^\circ\text{C}$ in proposed He-cooled divertor designs and $>1700^\circ\text{C}$ in the divertor armour surface [12], whereas neutron bombardment is

1
2
3
4
5
6
7
8
9
10
11
12
13
14
15
16
17
18
19
20
21
22
23
24
25
26
27
28
29
30
31
32
33
34
35
36
37
38
39
40
41
42
43
44
45
46
47
48
49
50
51
52
53
54
55
56
57
58
59
60
61
62
63
64
65

estimated to cause ~4 dpa in the W armour at the end-of-life of W-Cu plasma-facing components in DEMO [13].

Tungsten is characterised by a relatively low ductile-to-brittle-temperature (DBTT), namely ~200-400 °C [14-17], which can increase progressively with damage level due to the radiation fields inside the fusion reactor core up to ~800-1000 °C [18, 19]. Thermal cycling across the DBTT from temperatures between 70-120 °C up to the maximum surface temperature in W mock-ups during High-Heat-Flux (HHF) tests does not induce the formation of macro-cracks. However, macro-cracks are observed at a heat load of 20 MWm⁻² with the surface temperature approaching 2000 °C [3]. The highest temperature for safe operation of W components is limited by the resistance to creep, low-cycle fatigue, helium embrittlement and recrystallization [20, 21]. Mechanical test data at 800 °C constitute a representative property database for W monoblocks that is compared to their performance under HHF tests and is also used as key input for the universal slope method aimed at correlating tensile properties and fatigue performance of W monoblocks [3]. Plasma exposure of W-based PFCs causes radiation-induced lattice damage, surface sputtering, hydrogen isotope retention and He accumulation and diffusion into the bulk structure [22]. The latter effect can lead to bubble formation and potential blistering and, as a consequence, embrittlement at low temperatures and ductility loss at high temperatures [22]. Additionally, W exposure to He ions in the eV energy regime (>20-30 eV), where physical sputtering does not play a significant role in changes to surface morphology, at temperatures >700 °C and a minimal He fluence of ~10²⁵ m⁻² induces the formation of ‘nanostructured or fuzzy W’ on the material surface [5, 23, 24].

In this work we have applied extensive in-situ damage and microstructural analysis techniques to observe W and W-5wt.%Ta (W-5Ta) materials at 800 °C and exposed to 40 keV He⁺ irradiations at incremental damage levels from only 0.004 dpa up to 1 dpa with a

maximum He-to-dpa ratio of 5.5 at%/dpa. Tantalum alloying is one of the proposed engineering solutions to overcome the inherent drawbacks of W as a structural material, since Ta is reported to shift the onset of W recrystallization [25-28]. It has also been shown to reduce the vacancy mobility and to consequently delay void formation at 800 °C under proton irradiation [29]. In W-5Ta, voids were not found up to a damage level of 0.3 dpa, however, the excess of free vacancies present in the W-5Ta irradiated at 800°C led to the formation of visible voids in TEM study after post-irradiation annealing of the sample at 1000 °C. At lower temperatures the presence of Ta also retards the mobility of self-interstitial atoms (SIAs) and interstitial $a/2\langle 111 \rangle$ dislocation loops under irradiation at lower temperatures, and consequently the loop growth and coalescence, attaining saturation in loop dimensions at relatively low damage levels [30, 31]. Ta is also observed to hinder the surface blistering in W under high-fluence deuterium plasma irradiation [32]. In addition, dual beam and sequential irradiation experiments have shown to shift the fluence threshold for fuzz formation higher in W-Ta alloys at 950°C as the ratio of D^+/He^+ ions increases due to a significant D de-trapping at that temperature which led to the fast diffusion and escape of the implanted species [33]. The main research objective is to demonstrate the effect of the presence of Ta solute atoms in W-Ta binary system on response to radiation under cumulative helium beam exposure at an elevated temperature of 800 °C which remains largely unexplored. The results obtained in this work are important to the fusion community helping to expand the pallet of candidate structural materials for future fusion devices that are more resistant to He^+ induced surface damage. This data will also help to validate predictive models of the expected in-service degradation of fusion construction materials, so that more advanced alloy compositions with optimised properties can be designed and developed for the fusion reactors.

Materials

The initial 1 mm-thick W sheet (99.95%) was provided by Goodfellow Cambridge Ltd. The as-received W material was annealed in vacuum at 1400 °C for 2 h for recrystallization. The W-5Ta alloy was instead produced by Plansee AG via powder metallurgy. W-5Ta was double forged and then annealed at 1600 °C for 1 h [34]. After delivery, the material was annealed for 1 h at 1000 °C for degassing [35]. Afterwards, smaller samples of $2 \times 2 \text{ cm}^2$ were cut and also annealed at 1400 °C for 2 h to remove defects introduced during machining. After annealing, both W and W-5Ta materials were pre-thinned down to 80-100 μm in thickness using SiC abrasive papers from grit 220 up to 4000. TEM discs were then punched and electropolished at -5 °C using a Struers Tenupol-5 unit and an electrolyte comprising an aqueous solution of 0.5 wt.% Na_2S in the case of W, whereas a mixture of 15 vol.% H_2SO_4 (95%) and 85 vol.% CH_3OH was employed for W-5Ta. The average grain size was $3.9 \pm 0.8\text{mm}$ (W) and $2.3 \pm 0.7\text{mm}$ (W-5Ta) [29, 31].

Experimental

The samples were exposed sequentially to a 40 keV He^+ beam at the temperature of 800 °C, using the MIAMI-2 TEM/ion accelerator system located at the University of Huddersfield [36]. The in-situ TEM facility under ion irradiation is composed of a 300 kV Hitachi H-9500 Transmission Electron Microscope (TEM), coupled to a 350 kV NEC ion accelerator incorporating a Danfysik 921A ion source. The ion beam is incident on the sample at an angle of 18.7° to the electron beam in the TEM. Sample heating was achieved by a double-tilt heating holder (Gatan Model 652) that uses a current flow through a Ta furnace surrounding the sample. The temperature was measured via a thermocouple attached to the furnace. The sample was held in place using a Hexring® clamping mechanism to ensure good thermal contact between the sample and the furnace. On reaching the target temperature, the sample was irradiated by the He^+ beam in a series of steps from the lowest

1 damage level of 0.004 dpa up to 1 dpa at a rate of 4.5×10^{-4} dpa/s, corresponding to a He^+
2
3 fluence of 3.3×10^{14} and 7.3×10^{16} He^+/cm^2 respectively.
4

5 The simulated damage profile and the Helium concentration profile (Fig.1) were
6
7 calculated using the *Stopping and Range of Ions in Matter* (SRIM-13) software with the
8
9 quick Kinchin-Pease approach [37-39], using an average displacement energy of 90 eV [40]
10
11 and default values for other software settings. The total current deposited on the sample was
12
13 0.09 nA, with a He^+ flux of 3.3×10^{13} ions/ cm^2/s . It was predicted that over 50% of helium
14
15 ions was transmitted through the foil, and 32% was implanted. The damage level was
16
17 estimated as the average value in the foil thickness of $\sim 100 \pm 10\%$ nm, as determined by
18
19 Convergent Electron Beam Diffraction (CBED) prior to the experiment. Micrographs were
20
21 recorded along the zone axes $\langle 001 \rangle$ and $\langle 111 \rangle$ during the stepwise increase in He fluence,
22
23 starting at the lowest damage level of only 0.004 dpa. At damage steps representative of the
24
25 microstructure evolution, a through-focal series of micrographs was taken with a defocus
26
27 value $\Delta f \leq 1 \mu\text{m}$ in order to assess the presence of He bubbles ≥ 1 nm in diameter, based on the
28
29 “out-of-focus” Fresnel imaging technique [41].
30
31
32
33
34
35
36

37 Helium bubble detection

38
39 In order to determine the number and size of the bubbles in the image, the
40
41 topologically structured contour detection algorithm was applied from [42] as implemented in
42
43 the OpenCV Library [43]. Furthermore, a graphical user interface was developed in C++
44
45 using Qt Creator as a software development kit. The methodology for detection consisted of
46
47 three steps: generation of a binary image, contour estimation and area calculation.
48
49
50

51 The original TEM micrograph taken in under-focus condition was processed first
52
53 using Adobe Photoshop to enhance the bubbles out of the background via adjusting the
54
55 brightness and shadows and making small adjustments to individual colours with the hue and
56
57 saturation layers. Then determination of relative occupations of the surface by the helium
58
59
60
61
62
63
64
65

bubbles was specified after choosing suitable thresholds in ImageJ, version 1.53a [44]. In order to generate the binary image, the thresholded image was converted to grayscale (single-channel conversion). This followed by a fixed-level thresholding to determine whether a pixel is black or white, thus resulting in a binary representation of the image. The contour estimation algorithm provided a set of connecting pixels, contours, at the edges of the bubbles. The area of each contour was calculated using the Green's Theorem. Additionally, the centroid of each bubble was obtained by computing the image moment of its contour, this allowed to extract the area and centroid of each bubble, giving a full description of the location and size distribution of the bubbles in the micrograph. The images obtained at each of the main steps of bubble detection are shown in Fig. 2.

Results

Fig. 3 shows the evolution of the W microstructure at 800 °C as a function of damage level in the range of 0.01 up to 1 dpa, whereas the early stages of damage between 0.004 and 0.016 dpa are shown in Fig. 4. Comparatively, Fig. 5 shows the radiation-induced damage in W-5Ta in the same damage range as in W in Fig. 3. In both materials, the damaged structure is characterised by a population of helium bubbles that change in density, size and morphology with increasing damage level up to the maximum value of 1 dpa in this work. Fig. 6 displays the evolution of the average bubble size and the number density as it relates to damage level in both materials. The radiation-induced dislocation loops were not detected in any of these materials at 800 °C. A significant number of spherical bubbles of >1 nm in diameter are already present in W at the relatively low damage level of 0.004 dpa, which corresponds to a He^+ fluence of $3.3 \times 10^{14} \text{ He}^+/\text{cm}^2$. Both the average bubble size and density increase continuously up to a damage level of 0.2 dpa, where the average size reaches ~3nm and the density amounts to $\sim 26 \times 10^{22}/\text{m}^3$. At higher damage levels, both the average size and density continue increasing but at a lower rate, and do not reach saturation at the end of the

experiment. At the maximum damage level of 1 dpa, the average size of the bubble population is 3.9(3) nm and the density is $\sim 32 \times 10^{22}/\text{m}^3$. Additionally, at damage levels ≥ 0.3 dpa, the He bubbles gradually change their morphology from spherical to faceted (see insets in Fig. 3 and Fig. 7a). In contrast, there are no visible bubbles in W-5Ta below 0.02 dpa, and the bubble density remains low up to 0.1 dpa. Between 0.1 and 0.2 dpa, there is a sharp increase in bubble density. At >0.2 dpa the density continues to rise at a lower rate than before but still higher than in W and reaches a value of $\sim 31 \times 10^{22}/\text{m}^3$, which is close to the bubble density in W at the same damage level. Additionally, the average bubble size in W-5Ta undergoes a smaller increase with damage level and seems to saturate at 2.2(3) nm at 1 dpa. That size value is ~ 1.7 times smaller than the value measured in W also at 1 dpa. At such damage level, most of the He bubbles in W-5Ta still remain largely spherical (see Fig. 7b). Figure 8 plots the size frequency distribution of helium bubbles showing an increase in size as a function of a damage level up to 1 dpa. The histograms reveal a shift in bubble sizes limited to a maximum of <3.5 nm and a peak frequency at <2.5 nm in W-5Ta and a maximum of <5 nm and a peak frequency at <4 nm in W at 1 dpa.

Discussion

The helium irradiated microstructure of W at 800 °C is characterised by the presence of a relatively large number of bubbles, whose average size and bubble density change with an increase of a damage level, and addition of Ta content. There was no evidence of dislocation loops at 800 °C. This is supported with data on tungsten-rhenium alloys irradiated with neutrons and tungsten-tantalum alloys irradiated with protons at temperatures up to 800 °C [29, 45]. The interstitial dislocation loops would be unstable at this elevated temperature and emit self-interstitial atoms, or glide to the free sample surface. Whereas, tungsten sample irradiated with neutrons at $T < 750$ °C and a damage level of <1 dpa are characterised by the presence of dislocation loops, whereas at higher irradiation temperatures

the irradiated microstructure is dominated by the presence of nm-sized voids and the absence of loops [46]. Generally, both W and W-Ta exhibit microstructures with $\leq 20\%$ of the area occupied by the radiation-induced bubbles under 40 keV He^+ exposure up to 1 dpa. The helium fluence was reported to exhibit a very limited impact on bubble size in W at $T < 1200^\circ\text{C}$. In tungsten irradiated at 800°C by 10 keV helium ions, the average bubble density was found to be around $(3.0\text{--}4.0) \times 10^{16} \text{m}^{-2}$, and the mean bubble size was reported to be between 2.0 nm and 3.5 nm which is similar to results obtained in this work ($\sim 2 \times 10^{16} \text{m}^{-2}$) [47].

Helium atom diffusion is the principal factor affecting the helium bubble nucleation and growth processes. Helium has an extremely low solubility and low migration energy in metals [48]. The irradiation temperature 800°C in this work corresponds to the annealing stage IV reported to occur in W between $650\text{--}1000^\circ\text{C}$, when the radiation-induced vacancies become mobile [49]. In tungsten, substitutional helium atoms tend to form various strong complexes with vacancies, which are considered as the nuclei of the helium bubbles, which preferentially grow by further helium and helium-vacancy absorption [50]. DFT calculations showed that helium will migrate to vacancies rather than remain in interstitial or substitutional sites [51]. Helium atoms are strongly bound with the vacancies because they compensate its negative volume dilatation [52]. The energy barrier was estimated and reported to be quite high (2.8 eV) for a possibility of a direct jump of the He atom from one vacancy to another in W, supposing a great trapping effect between He and the vacancy in W [53]. At temperatures $> 600^\circ\text{C}$ mobility of the He vacancy complexes is reported to increase, which leads to the development of larger (greater than several nanometres) bubbles [54]. Ultimately these implanted He atoms that are trapped at vacancies may cause helium embrittlement of the material.

Diffusion in an alloy is more complex than in a single element component where vacancy-helium atom clustering might be retarded due to the existence of solute dopants. The first-principle calculations revealed a repulsive Ta solute-vacancy interaction in W with a binding energy between Ta and a monovacancy from -0.1 to -0.3 eV for the first-to-third nearest-neighbour positions. However, a weak attractive interaction was reported for Ta atom on the neighbouring position perpendicular to the $\langle 111 \rangle$ crowdion, resulting in the impeded diffusion of the SIA [55]. Therefore, the solute Ta partly increases the recombination of vacancy with interstitial, and decreases the concentration of point defects, thereby, leading to a reduced vacancy concentration within the matrix. Moreover, the binding energy between a Ta interstitial atom and a He atom in W, when He was initially situated in the third to first nearest-neighbour sites relatively to a Ta atom, was reported to be 0.1-0.3 eV, and the binding energy between the second introduced He atom and existing He-Ta complex was declared to be 1.1 eV. This indicates a strong favourable binding effect and consequent trapping of He by substitutional Ta or already formed He-Ta complexes preventing He atom migration in the W lattice [56]. The consequence of the described above events is a lower probability of interaction between vacancies and He atoms in the vicinity of tantalum atoms.

In addition, the formation energy of a mono-vacancy for the first-to-fourth nearest-neighbour positions in W-5Ta alloy was reported to be higher compared to the pure tungsten, suggesting that mono-vacancies are not that easily formed around the Ta atom in W [57]. delaying vacancy diffusion via a solute drag effect [58], which may retard the vacancy mobility and further binding of a vacancy with He in W. The formation energy of a He interstitial in the W-5Ta alloy, with the most stable configuration for He in the substitution site, was reported to be lower (4.56 eV) and therefore more favourable compared to the pure tungsten system (4.92 eV) [59]. The formation energies of the He atom in the tetrahedral interstitial site and octahedral interstitial site were also calculated in pure W and were

1 reported to be 6.18 and 6.43 eV which is also higher than in W-Ta alloy (5.50 and 5.84 eV
2 respectively). The helium-vacancy clustering and the ability of bubble formation and their
3 further growth is therefore retarded in the W-Ta system below 0.02 dpa. Whereas in contrast,
4 already at a damage level of 0.004 dpa, small bubbles of >1 nm have been detected in W
5 yielding the density of $4.2 \times 10^{20} \text{ m}^{-3}$. Hence, the presence of Ta interferes with
6 helium/vacancy clustering and subsequently delays bubble nucleation causing deceleration of
7 the bubble transition into faceted shape at higher damage levels.
8
9

10 A similar trend in the radiation-induced defect retention was observed in W-5Ta
11 irradiated in-situ by 40 keV protons at 800°C [29, 60]. In comparison with the growing
12 number of voids in W, the voids in W-5Ta were not detected up to a damage level of
13 0.3 dpa, however, the proton irradiation-induced voids became visible when the same sample
14 was post-irradiation annealed at 1000 °C, with a relatively low void density of $4.9 \pm 1.4 \times$
15 10^{21} m^{-3} and an average size of $4.9 \pm 1.4 \text{ nm}$, occurring as a result of the agglomeration of
16 voids by a thermally activated process [29]. And the exposure of W-5Ta to a lower energy of
17 100 eV He^+ ions showed similar behaviour with surface fuzz, a result of defect mobility
18 being suppressed in comparison to unalloyed W due to the bigger lattice spacing forced by
19 doping of W with Ta [33, 61]. The higher fluence threshold for the formation of surface
20 nano-structuring implies that the W-Ta alloy's surface thermal conductivity will degrade at a
21 slower rate compared to the pure W system during the lifespan of a reactor [62].
22
23
24
25
26
27
28
29
30
31
32
33
34
35
36
37
38
39
40
41
42
43
44
45

46 The surface effect needs to be taken into account during the in-situ irradiations,
47 especially when the TEM foil thickness is <100 nm [63]. The free surface effect was
48 previously observed on the dislocation structure due to the thin foil in the in-situ experiment
49 [31]. The ex-situ TEM analysis revealed the coexistence of dislocation tangles and loops in
50 both materials, as opposed to the lack of dislocation tangles in the in-situ specimens.
51 Furthermore there was no change in the nature (i.e. interstitial to vacancy type) of the
52
53
54
55
56
57
58
59
60
61
62
63
64
65

dislocation loops and their Burgers vector, and a significant number of vacancy clusters was also not present, but we did observe the appearance of dislocation tangles in the ex-situ samples. The ex-situ irradiation of bulk tungsten with He ions of 400 keV showed the formation of larger bubble diameters (>10 nm) but lower areal bubble density ($\sim 10^{16}$ bubbles/m²) compared to the in-situ experiments. This was due to higher amounts of He retained in the irradiated bulk materials while in the in-situ experiments on thin foils some may escape due to the proximity of surfaces [64]. In addition, at higher irradiation temperature the diffusivity ratio of point defect is greater [63]. Hence, considering the influence of the surface effect, the population of the helium bubbles measured in the thin TEM foils is lower than the actual value in bulk would be.

At a damage level ≥ 0.3 dpa, the bubbles present in W develop energetically favourable facets with the facet planes of $\{110\}$, as interpreted by the anisotropy of the surface energy and by the preferential adsorption of diffusing helium ions on specific plane orientations with respect to the bubble surface. The descending order of surface energies in bcc is for low-index planes $\{111\}$, $\{100\}$, and $\{110\}$ with the lowest surface energy for the planes $\{110\}$ due to the greater planar density [65]. To minimize the total free energy, the facets with the lowest surface energy occupy most of the bubble surface along $\{110\}$. The fraction of the faceted bubbles in W rises and amounts to $>80\%$ at a maximum of 1 dpa. However, the spherical-to-faceted transition of bubble shape is clearly suppressed in W-5Ta alloy.

Conclusions

In-situ analysis of helium bubble formation has been performed in W and W-5Ta alloy, caused by 40 keV He⁺ irradiation at 800°C up to 1 dpa with a maximum He-to-dpa ratio of 5.5 at%/dpa. The extensive use of advanced in-situ TEM characterizations showed the effect of helium fluence and alloying component on the structural morphology of the

helium bubbles. The spherical bubbles of >1 nm were observed in W at the relatively low damage level of 0.004 dpa, which corresponds to a He⁺ fluence of 3.3×10^{14} He⁺/cm². The presence of only 5wt.%Ta in solid solution impedes the diffusion of helium ions at 800 °C and interferes with the binding of He ions with vacancies into complexes, which serve as the core of a helium bubble, and therefore hinders the nucleation of the bubbles <0.02 dpa. Moreover, at 1 dpa, >80% of the bubbles in W steadily develops facets, whereas in contrast in W-5Ta bubbles still present a spherical shape.

Acknowledgements

The authors of this work acknowledge Prof S. E. Donnelly for access to the MIAMI-2 facility (grant ref. EPSRC EP/M028283/1) through the EPSRC funded mid-range facility, the UK National Ion Beam Centre (NS/A000059/1). Authors I.I., M.J.D.R. and S.C.M. are supported through the Sêr Cymru Nuclear Futures Institute funded through WEFO (Wales).

References

- [1] V. Philipps, Tungsten as material for plasma-facing components in fusion devices, *J. Nucl. Mater.* 2011, **415**, S2-S9.
- [2] D. Stork, P. Agostini, J.L. Boutard, D. Buckthorpe, E. Diegele, S.L. Dudarev, et al., Developing structural, high-heat flux and plasma facing materials for a near-term DEMO fusion power plant: The EU assessment, *J. Nucl. Mater.* 2014, **455**, 277-291.
- [3] T. Hirai, S. Panayotis, V. Barabash, C. Amzallag, F. Escourbiac, A. Durocher, et al., Use of tungsten material for the ITER divertor, *Nucl. Mater. Ener.* 2016, **9**, 616-622.
- [4] V. A. Soukhanovskii, A review of radiative detachment studies in tokamak advanced magnetic divertor configurations, *Plasma Phys. Control. Fusion.* 2017, **59**, 064005.
- [5] Y. Ueda, J.W. Coenen, G. De Temmerman, R.P. Doerner, J. Linke, V. Philipps, E. Tsitrone, Research status and issues of tungsten plasma facing materials for ITER and beyond, *Fusion Eng. Des.* 2014, **89**, 901-906.

- [6] R. Villari, V. Barabash, F. Escourbiac, L. Ferrand, T. Hirai, V. Komarov, et al., Nuclear analysis of the ITER full-tungsten divertor, *Fusion Eng. Des.* 2013, **88**, 2006-2010.
- [7] F. Crescenzia, C. Bachmann, M. Richou, S. Roccella, E. Visca, J.-H. You, Design study of ITER-like divertor target for DEMO, *Fusion Eng. Des.* 2015, **98-99**, 1263-1266.
- [8] H. Reimerdes, R. Ambrosino, P. Innocente, A. Castaldo, P. Chmielewski, G. Di Gironimo, et al., Assessment of alternative divertor configurations as an exhaust solution for DEMO, *Nucl. Fusion*. 2020, **60**, 066030.
- [9] S. Heuer, Th Weber, G. Pintsuk, J.W. Coenen, J. Matejicek, Ch Linsmeier, Aiming at understanding thermo-mechanical loads in the first wall of DEMO: stress-strain evolution in a Eurofer-tungsten test component featuring a functionally graded interlayer, *Fusion Eng. Des.* 2018, **135**, 141-153.
- [10] T.R. Barrett, G. Ellwood, G. Pérez, M. Kovari, M. Fursdon, F. Domptail, et al., Progress in the engineering design and assessment of the European DEMO first wall and divertor plasma facing components, *Fusion Eng. Des.* 2016, **109-111**, 917-924.
- [11] P. Sardain, B. Michel, L. Giancarli, A. Li Puma, Y. Poitevin, J. Szczepanski, et al. *Fusion Eng. Des.* 2003, **69**, 769-774.
- [12] M. Rieth, S.L. Dudarev, S.M. Gonzalez de Vicente, J. Aktaa, T. Ahlgren, S. Antusch, et al., *J. Nucl. Mater.* 2013, **442**, S173-S180.
- [13] M. Barbarino, A. Leonard, N.N. Asakura, M. Jakubowski, M. Kobayashi, B. Lipschutz, et al., Summary of the 3rd IAEA technical meeting on divertor concepts, *Nucl. Fusion* (In Press).
- [14] T. Shen, Y. Dai, Y. Lee, Microstructure and tensile properties of tungsten at elevated temperatures, *J. Nucl. Mater.* 2016, **468**, 348-354.
- [15] P. Gumbsch, Brittle fracture and the brittle-to-ductile transition of tungsten, *J. Nucl. Mater.* 2003, **323**, 304-312.

- [16] B. Gludovatz, S. Wurster, A. Hoffmann, R. Pippan, Fracture toughness of polycrystalline tungsten alloys, *Int. J. Refract. Metals Hard Mater.* 2010, **28**, 674-678.
- [17] E. Gaganidze, D. Rupp, J. Aktaa, Fracture behaviour of polycrystalline tungsten, *J. Nucl. Mater.* 2014, **446**, 240-245.
- [18] H. Bolt, V. Barabash, G. Federici, J. Linke, A. Loarte, J. Roth, K. Sato, Plasma facing and high heat flux materials – Needs for ITER and beyond, *J. Nucl. Mater.* 2002, **307-311**, 43-52.
- [19] I.V. Gorynin, V.A. Ignatov, V.V. Rybin, S.A. Fabritsiev, V.A. Kazakov, V.P. Chakin, et al., Effects of neutron irradiation on properties of refractory metals, *J. Nucl. Mater.* 1992, **191-194**, 421-425.
- [20] S.J. Zinkle, N.M. Ghoniem, Operating temperature windows for fusion reactor structural Materials, *Fusion Eng. Des.* 2000, **51-52**, 55-71.
- [21] N. Baluc, Materials for fusion power reactors, *Plasma Phys. Control. Fusion* 2006, **48**, B165–B177.
- [22] N. Yoshida, Review of recent works in development and evaluation of high-Z plasma facing materials, *J. Nucl. Mater.* 1999, **266-269**, 197-206.
- [23] M.J. Baldwin, R.P. Doerner, Formation of helium induced nanostructure “fuzz” on various tungsten grades, *J. Nucl. Mater.* 2010, **404**, 165.
- [24] S. Kajita, W. Sakaguchi, N. Ohno, N. Yoshida, T. Saeki, Formation process of tungsten nanostructure by the exposure to helium plasma under fusion relevant plasma conditions, *Nucl. Fusion* 2009, **49**, 095005.
- [25] M. Rieth, S.L. Dudarev, S.M. Gonzalez de Vicente, J. Aktaa, T. Ahlgren, S. Antusch, et al., A brief summary of the progress on the EFDA tungsten materials program, *J. Nucl. Mater.* 2013, **442**, S173-S180.

- [26] E.Tejado, P.A.Carvalho, A.Muñoz, M.Dias, J.B.Correia, U.V.Mardolcar, J.Y.Pastor, The effects of tantalum addition on the microtexture and mechanical behaviour of tungsten for ITER applications, *J. Nucl. Mater.* 2015, **467**, 949.
- [27] D. Jiang, Q. Wang, W. Hu, Z. Wei, J. Tong, H. Wan, The effect of tantalum (Ta) doping on mechanical properties of tungsten (W): a first-principles study, *J. Mater. Res.* 2016, **31**, 3401-3408.
- [28] Z. Wang, Y. Yuan, K. Arshad, J. Wang, Z. Zhou, J. Tang, G.-H. Lu, Effects of tantalum concentration on the microstructures and mechanical properties of tungsten-tantalum alloys, *Fusion Eng. Des.* 2017, **125**, 496-502.
- [29] I. Ipatova I, R.W. Harrison, S.E. Donnelly, M.J.D. Rushton, S.C. Middleburgh, E. Jimenez-Melero, Void evolution in tungsten and tungsten-5wt.% tantalum under in-situ proton irradiation at 800 and 1000 °C, *J. Nucl. Mater.* 2019, **526**, 151730.
- [30] X. Yi, M.L. Jenkins, K. Hattar, P.D. Edmondson, S.G. Roberts, Characterisation of radiation damage in W and W-based alloys from 2 MeV self-ion near-bulk implantations, *Acta Mater.* 2015, **92**, 163.
- [31] I. Ipatova, R.W. Harrison, P.T. Wady, S.M. Shubeita, D. Terentyev, S.E. Donnelly, E. Jimenez-Melero, Structural defect accumulation in tungsten and tungsten-5wt.% tantalum under incremental proton damage, *J. Nucl. Mater.* 2018, **501**, 329.
- [32] H. Zhou, J. Yu, W. Han, L. Cheng, C. Chen, K. Zhu, Large plastic deformation blistering and helium retention in 5% tantalum doped tungsten under 60 keV helium ions implantation, *Fus. Eng. Des.* 2018, **134**, 43-50.
- [33] S. Gonderman, J.K. Tripathi, T. Sizyuk, A. Hassanein, Suppression of surface microstructure evolution in W and W-Ta alloys during simultaneous and sequential He and D ion irradiation in fusion relevant conditions, *Nucl. Fusion.* 2017, **57**, 086001.

- [34] J. Linke, T. Loewenhoff, V. Massaut, G. Pintsuk, G. Ritz, M. Rödig, et al., Performance of different tungsten grades under transient thermal loads, *Nucl. Fusion*. 2011, **51**, 073017.
- [35] Y. Zayachuk, M.H.J. t Hoen, P.A. Zeijlmans van Emmichoven, D. Terentyev, I. Uytendhouwen, G. van Oost, Surface modification of tungsten and tungsten-tantalum alloys exposed to high-flux deuterium plasma and its impact on deuterium retention, *Nucl. Fusion*. 2013, **53**, 013013.
- [36] G. Greaves, A.H. Mir, R.W. Harrison, M.A. Tunes, S.E. Donnelly, J.A. Hinks, New Microscope and Ion Accelerators for Materials Investigations (MIAMI-2) system at the University of Huddersfield, *Nucl. Instr. Meth. Phys. Res. A*. 2019, **931**, 37-43.
- [37] J.F. Ziegler, Stopping of energetic light ions in elemental matter, *J. Appl. Phys.* 1999, **85**, 1249-1272.
- [38] J.F. Ziegler, M.D. Ziegler, J.P. Biersack, SRIM e the stopping and range of ions in matter (2010), *Nucl. Instrum. Methods Phys. Res. B*. 2010, **268**, 1818-1823.
- [39] R.E. Stoller, M.B. Toloczko, G.S. Was, A.G. Certain, S. Dwaraknath, F.A. Garner. On the use of SRIM for computing radiation damage exposure. *Nucl. Instr. Meth. Phys. Res. B*. 2013, **310**, 75-80.
- [40] ASTM E521-96, Standard Practice for Neutron Radiation Damage Simulation by Charged-Particle Irradiation, 2009.
- [41] M.L. Jenkins, M.A. Kirk, Characterization of Radiation Damage by Transmission Electron Microscopy, *IOP Publishing Ltd*. 2001.
- [42] S. Suzuki, K. Abe, Topological structural analysis of digitized binary images by border following, *Computer Vision, Graphics, and Image Processing*. 1985, **30**, 32-46
- [43] G. Bradski, The OpenCV Library, *Dr. Dobb's Journal of Software Tools*. 2000.
- [44] C.A. Schneider, W.S. Rasband, K.W. Eliceiri, NIH Image to ImageJ: 25 years of image analysis. *Nat. Methods*. 2012, **9**, 671-675.

- [45] M. Fukuda, K. Yabuuchi, S. Nogami, A. Hasegawa, T. Tanaka, Microstructural development of tungsten and tungsten–rhenium alloys due to neutron irradiation in HFIR, *J. Nucl. Mater.* 455 (2014) 460–463.
- [46] A. Hasegawa, M. Fukuda, S. Nogami, K. Yabuuchi, Neutron irradiation effects on tungsten materials, *Fusion Eng. Des.* 89 (2014) 1568–1572
- [47] X. Yi, K. Arakawa, D. Nguyen-Manh, F. Ferroni, P. Liu, W. Han, et al., A study of helium bubble production in 10 keV He⁺ irradiated tungsten. *Fus. Eng. Des.* 2017, **125**, 454-457.
- [48] H. Iwakiri, K. Yasunaga, K. Morishita, and N. Yoshida, Microstructure evolution in tungsten during low-energy helium ion irradiation, *J. Nucl. Mater.* 2000, **283-287**, 1134-1138.
- [49] L.K. Keys, J. Moteff, Neutron irradiation and defect recovery of tungsten, *J. Nucl. Mater.* 1970, **34**, 260-280.
- [50] X.C. Li, Y.-N. Li, Y. Yu, G.-N. Luo, X. Shu, G.-H. Lu, Helium defects interactions and mechanism of helium bubble growth in tungsten: A molecular dynamics simulation, *J. Nucl. Mater.* 2014, **451**, 356-360.
- [51] S.-C. Lee, J.-H. Choi, J. G. Lee, Energetics of He and H atoms with vacancies in tungsten: First-principles approach, *J. Nucl. Mater.* 2009, **383(3)**, 244-246.
- [52] G. D. Samolyuk, Y. N. Osetsky & R. E. Stoller, Properties of Vacancy Complexes with Hydrogen and Helium Atoms in Tungsten from First Principles, *Fusion Sc. Technol.* 2017, **71**, 52-59.
- [53] C. González and R. Iglesias, “Migration mechanisms of helium in copper and tungsten,” *J. Mater. Sci.*, vol. 49, no. 23, pp. 8127–8139, 2014.

- [54] Y. Ueda, J.W. Coenen, G. De Temmerman, R.P. Doerner, J. Linke, V. Philipps, et al., Research status and issues of tungsten plasma facing materials for ITER and beyond. *Fus. Eng. Des.* 2014, **89**, 901-906.
- [55] X.-S. Kong, X. Wu, Y.-W. You, C.S. Liu, Q.F. Fang, J.-L. Chen et al., First-principles calculations of transition metal–solute interactions with point defects in tungsten. *Acta Mater.* 2014, **66**, 172-183.
- [56] X. Wu, X.-S. Kong, Y.-W. You, C.S. Liu, Q.F. Fang, J.-L. Chen et al., Effects of alloying and transmutation impurities on stability and mobility of helium in tungsten under a fusion environment. *Nucl. Fusion.* 2013, **53**, 073049-073058.
- [57] S. Wen, K. Hu, M. Pan et al., Effect of transmutation elements Re and Ta on the vacancy formation and dissociation behaviors in W bulk. *Comput. Mater. Sci.* 2020, **179**, 109624.
- [58] T. Garnier, M. Nastar, P. Bellon, D.R. Trinkle, Solute drag by vacancies in body-centered cubic alloys. *Phys. Rev.* 2013, **B 88**, 134201.
- [59] C. Wan, S. Yu, X. Ju, W. Wang, Hydrogen trapping in helium-implanted W and W-Ta alloy: First-principles approach. *J. Nucl. Mater.* 2018, **508**, 249-256.
- [60] F.A. Smidt Jr., J.A. Sprague, Suppression of void nucleation by a vacancy trapping mechanism. *Scripta Metall.* 1973, **7**, 495-501.
- [61] S. Gonderman, J.K. Tripathi, T. Sizyuk, A. Hassanein, The effect of low energy helium ion irradiation on tungsten-tantalum (W-Ta) alloys under fusion relevant conditions, *J. Nucl. Mater.* 2017, **491**, 199-205.
- [62] T. Novakowski, J. Tripathi, A. Hassanein. Effect of high-flux, low-energy He⁺ ion irradiation on Ta as a plasma-facing material, *Sci. Rep.* 2016, **6**, 39746.
- [63] Y. Li, L. Wang, Y. Yuan, et al, In-situ TEM investigation of 30 keV he⁺ irradiated tungsten: Effects of temperature, fluence, and sample thickness on dislocation loop evolution, *Acta Mater.* 2021, 206, 116618.

[64] R.W. Harrison, N. Peng, R.P. Webb, et al, Characterisation of helium ion irradiated bulk tungsten: A comparison with the in-situ TEM technique, *Fusion Eng. Des.* 2019, 138, 210-216.

[65] E. Aghemenloh, J.O. Umukoro, S.O. Azi, S. Yusuf, J.O.A. Idiodi, Surface energy calculation of bcc metals using the analytical equivalent crystal theory method, *J. Nucl. Mater.* 2011, **50**, 3290-3296.

Figure captions

Fig. 1. Simulated damage and He⁺ concentration profiles in W at a damage level of 1 dpa to a He-to-dpa ratio of 5.5 at%/dpa, using the SRIM software with the quick Kinchin-Pease approach and the total current deposited on the sample in the experiment of 0.09 nA. The damage level was estimated at each step in the microstructure evolution as the average value in the foil thickness of ~100 nm. According to SRIM calculations, 32% of the 40keV He ions was implanted and 56% was transmitted through the foil.

Fig. 2. A series of images of helium bubbles observed in W at 800 °C and a damage level of 1 dpa through the main steps of the bubble detection: (a) bright-field image in under-focus condition, (b) thresholded image with enhanced bubbles, (c) grayscale binary image, (d) estimated contoured areas of detected bubbles

Fig. 3. In-situ observation of the bubble evolution W at 800 °C at selected damage levels up to 1 dpa induced by a 40 keV He⁺ ion beam: (a) 0.01 dpa, (b) 0.02dpa, (c) 0.05 dpa, (d) 0.075 dpa, (e) 0.1 dpa, (f) 0.2dpa, (g) 0.3 dpa, (h) 0.4 dpa, (i) 0.75 dpa, (j) 1 dpa. The insets show the bubble transition from spherical to faceted at ≥ 0.3 dpa. The TEM foil thickness was derived by way of the graphical method from the spacing of the fringes of the CBED patterns and was measured to be ~ 100 nm \pm 10%

Fig. 4. In-situ observation of bubble formation in W at 800 °C caused by a 40 keV He⁺ ion beam at the relatively low damage levels of: (a) 0.004 dpa, (b) 0.008 dpa, (c) 0.016 dpa. The TEM foil thickness was derived by way of the graphical method from the spacing of the fringes of the CBED patterns and was measured to be ~100 nm ± 10%

Fig. 5. In-situ observation of the bubble evolution W-5Ta at 800 °C at selected damage levels up to 1dpa induced by a 40 keV He⁺ ion beam: (a) 0.01 dpa, (b) 0.02dpa, (c) 0.04 dpa, (d) 0.05 dpa, (e) 0.1 dpa, (f) 0.2 dpa, (g) 0.3 dpa, (h) 0.4 dpa, (i) 0.75 dpa, (j) 1 dpa

Fig. 6. Average bubble size and bubble density in W and W-5Ta alloy at 800 °C as a function of damage level

Fig. 7. Bright field TEM image of spherical bubbles in W-5Ta and faceted bubbles in W, at 800 °C and the damage level of 1 dpa induced by a 40 keV He⁺ ion beam. The insets show the electron diffraction patterns taken along the zone axis <001> and <111>

Fig. 8 Frequency distribution histograms of helium bubble size showing an increase in size as a function of a damage level in W and W-5Ta irradiated with 40 keV He ions to a He-appm/dpa ratio of 55,000 and dose of 1 dpa

Figure 1

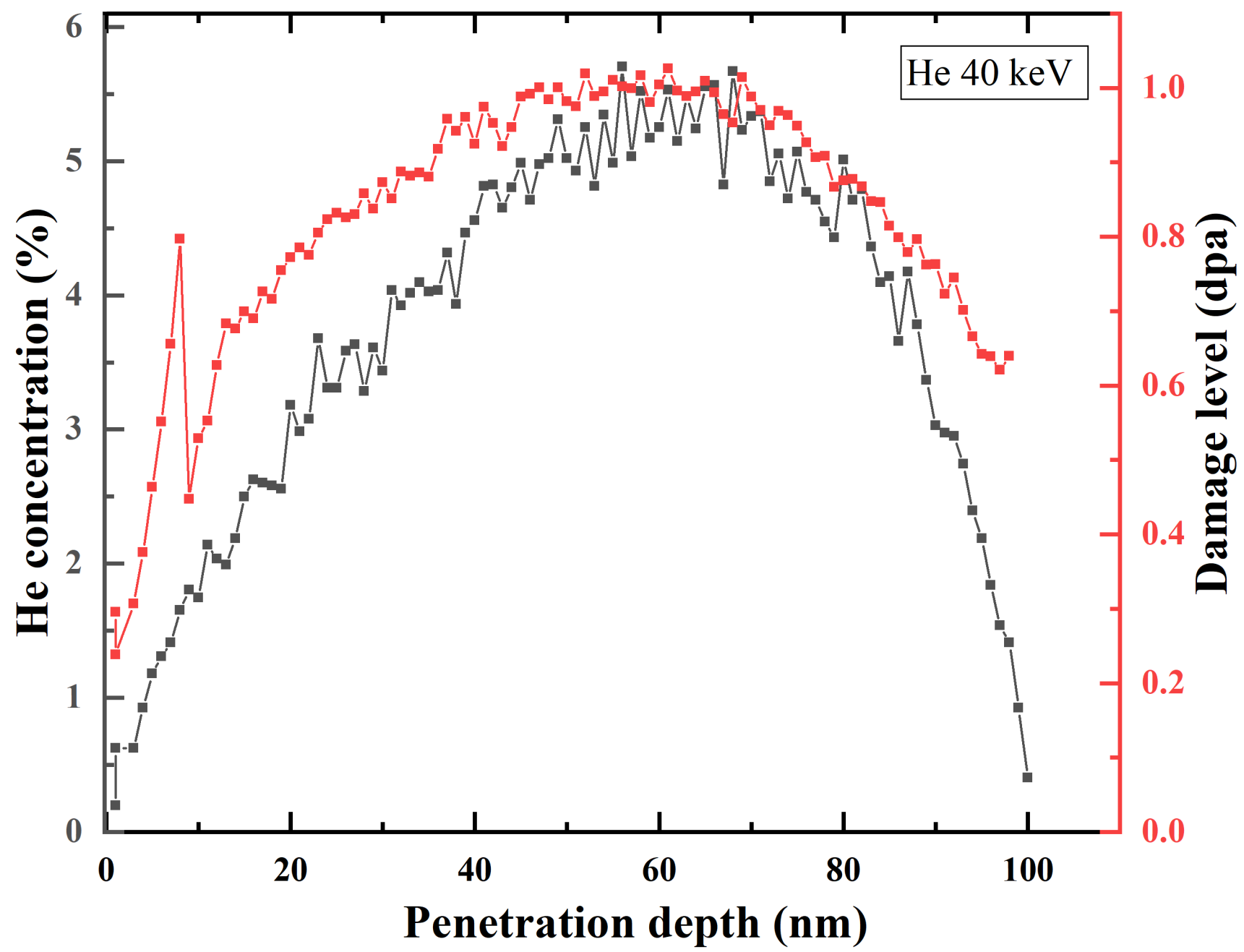
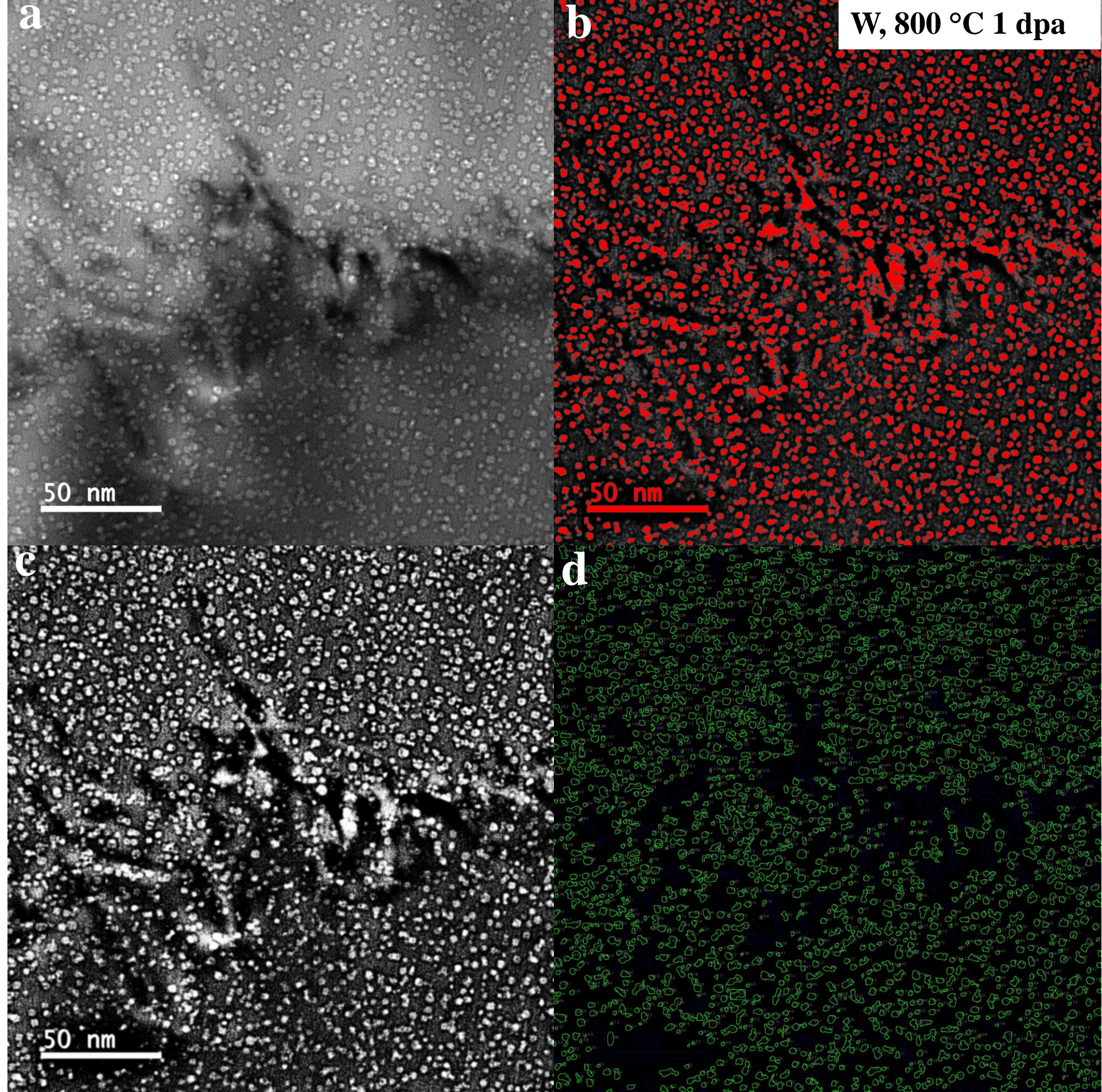
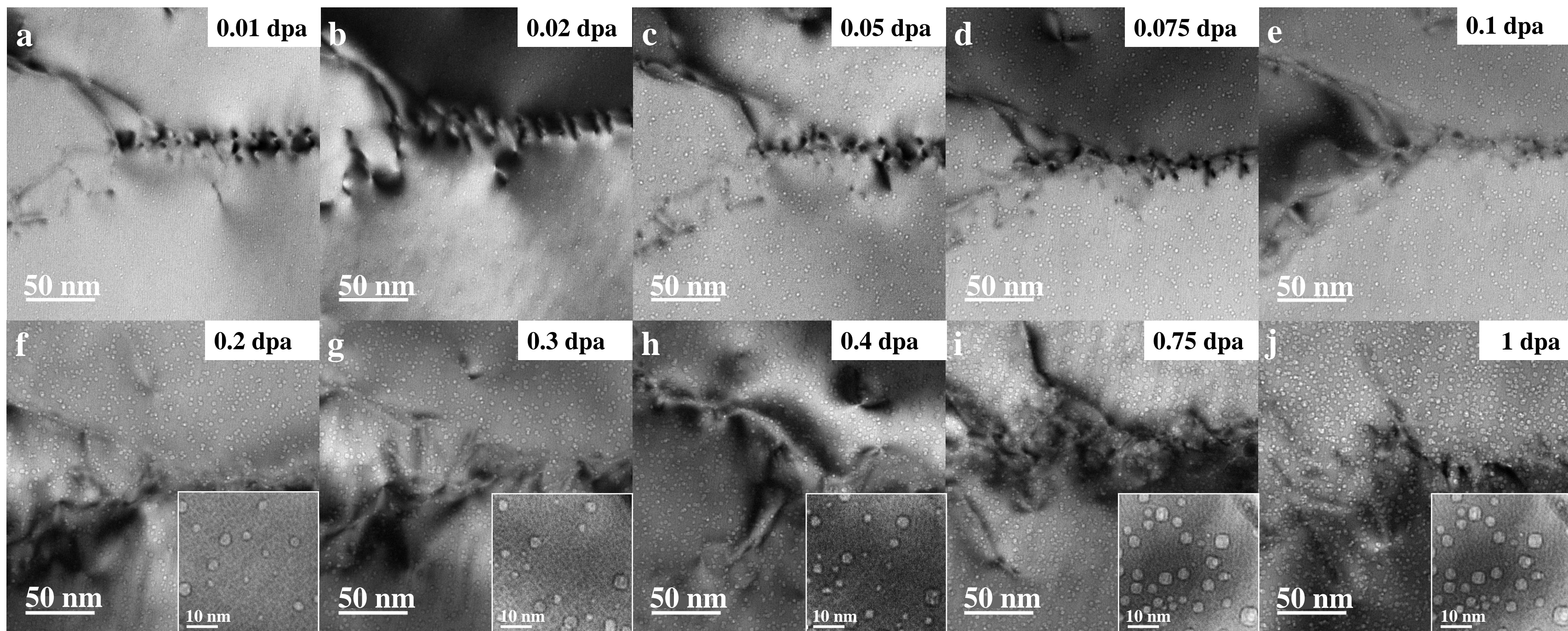
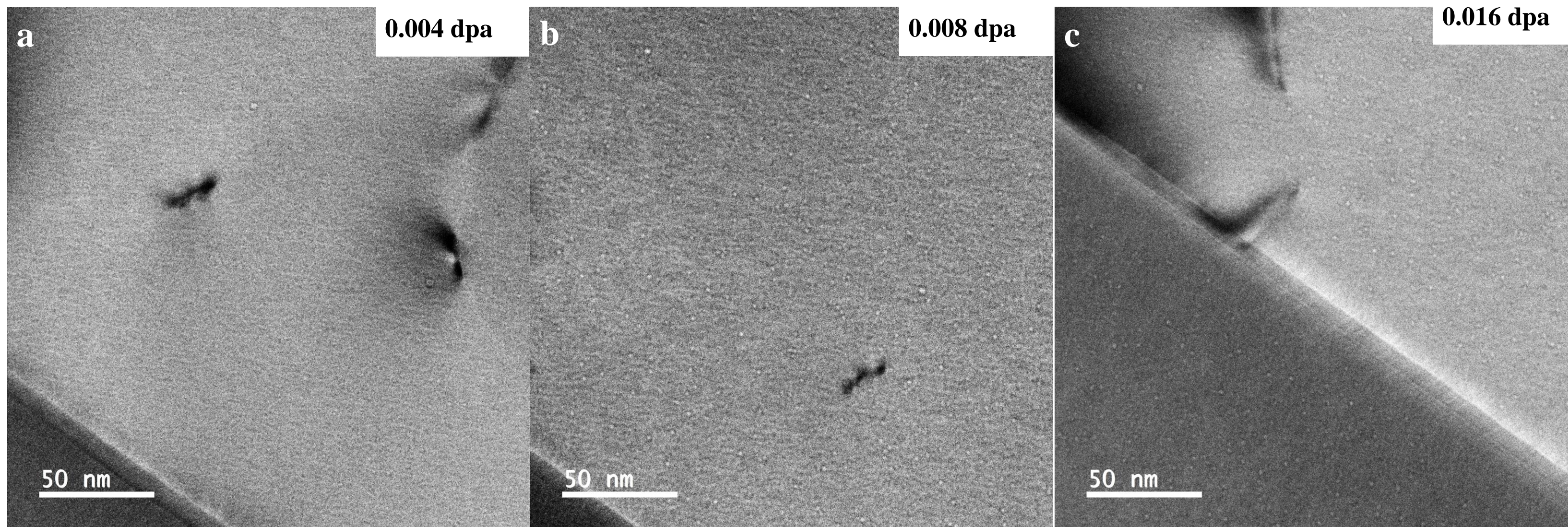
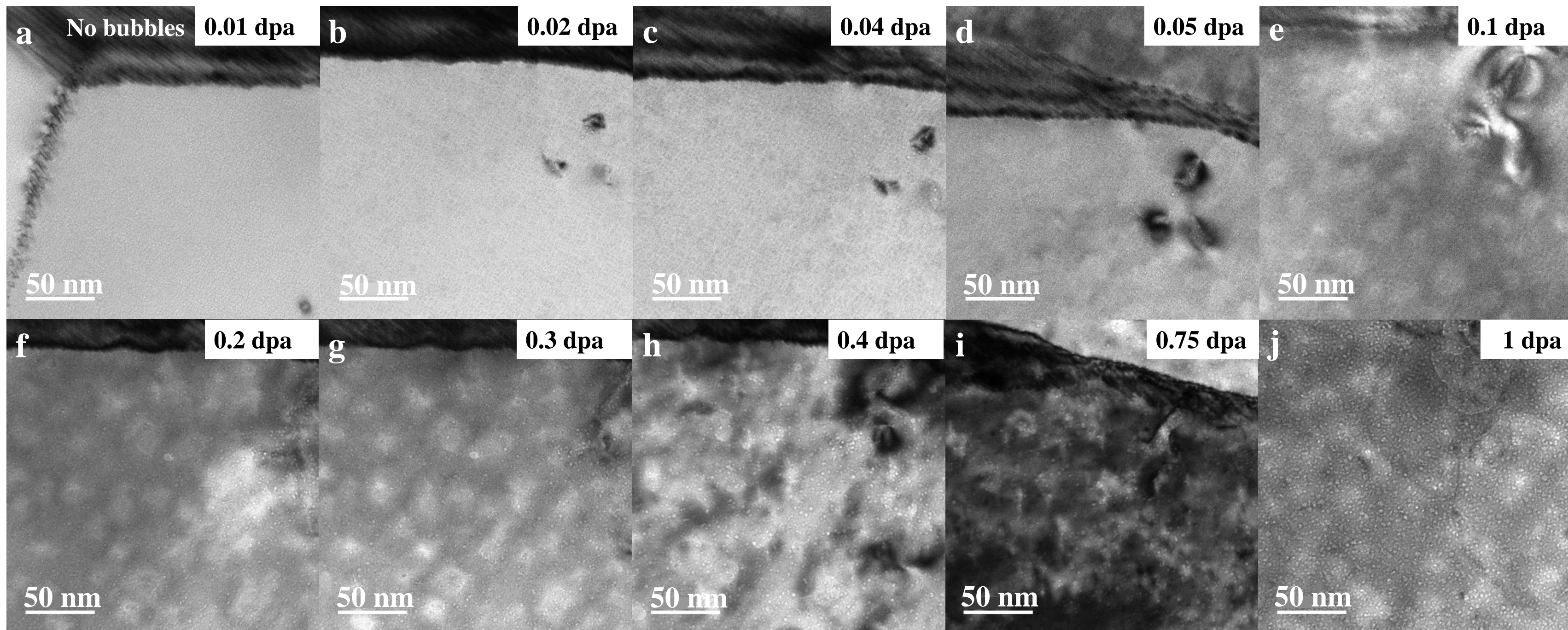


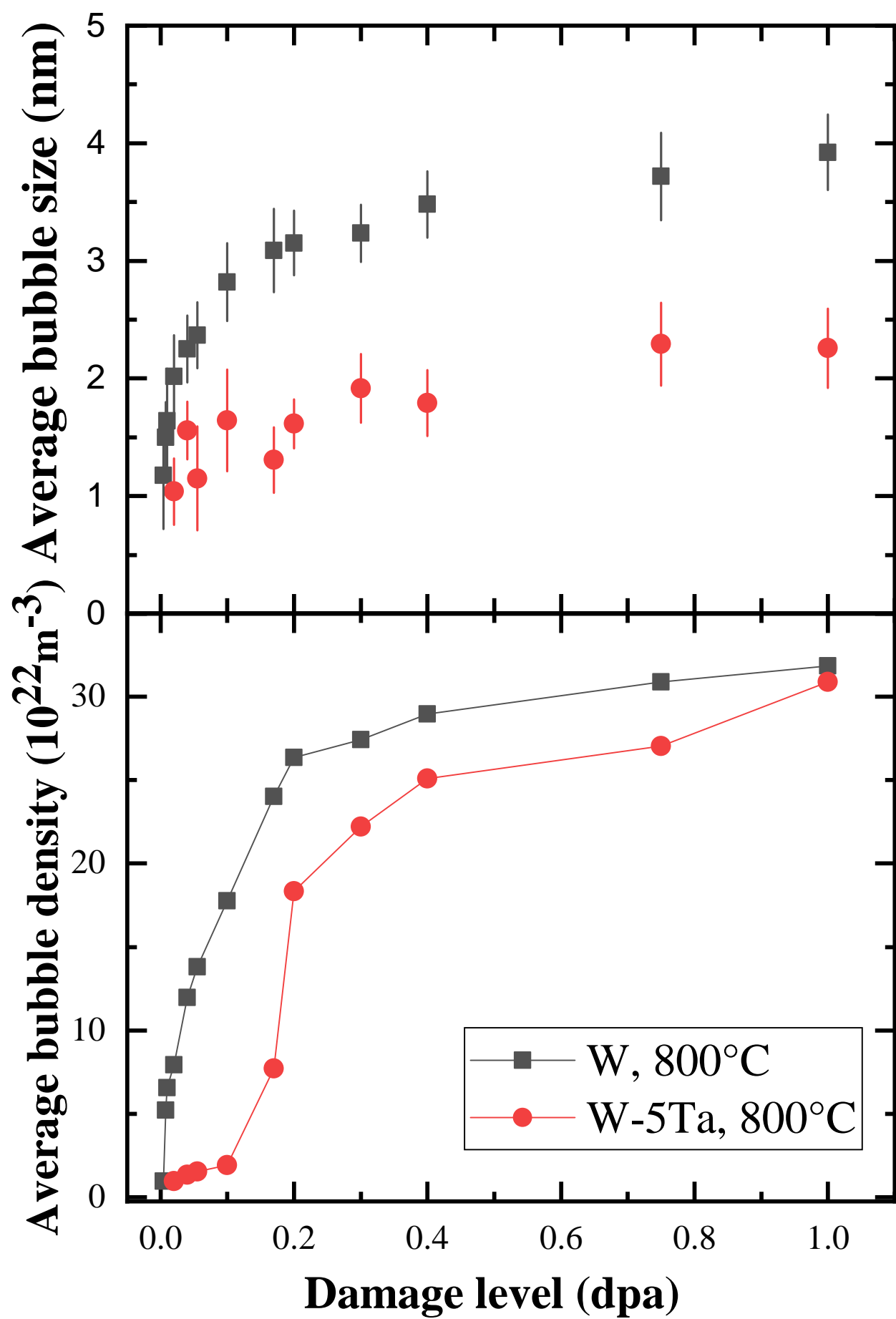
Figure 2











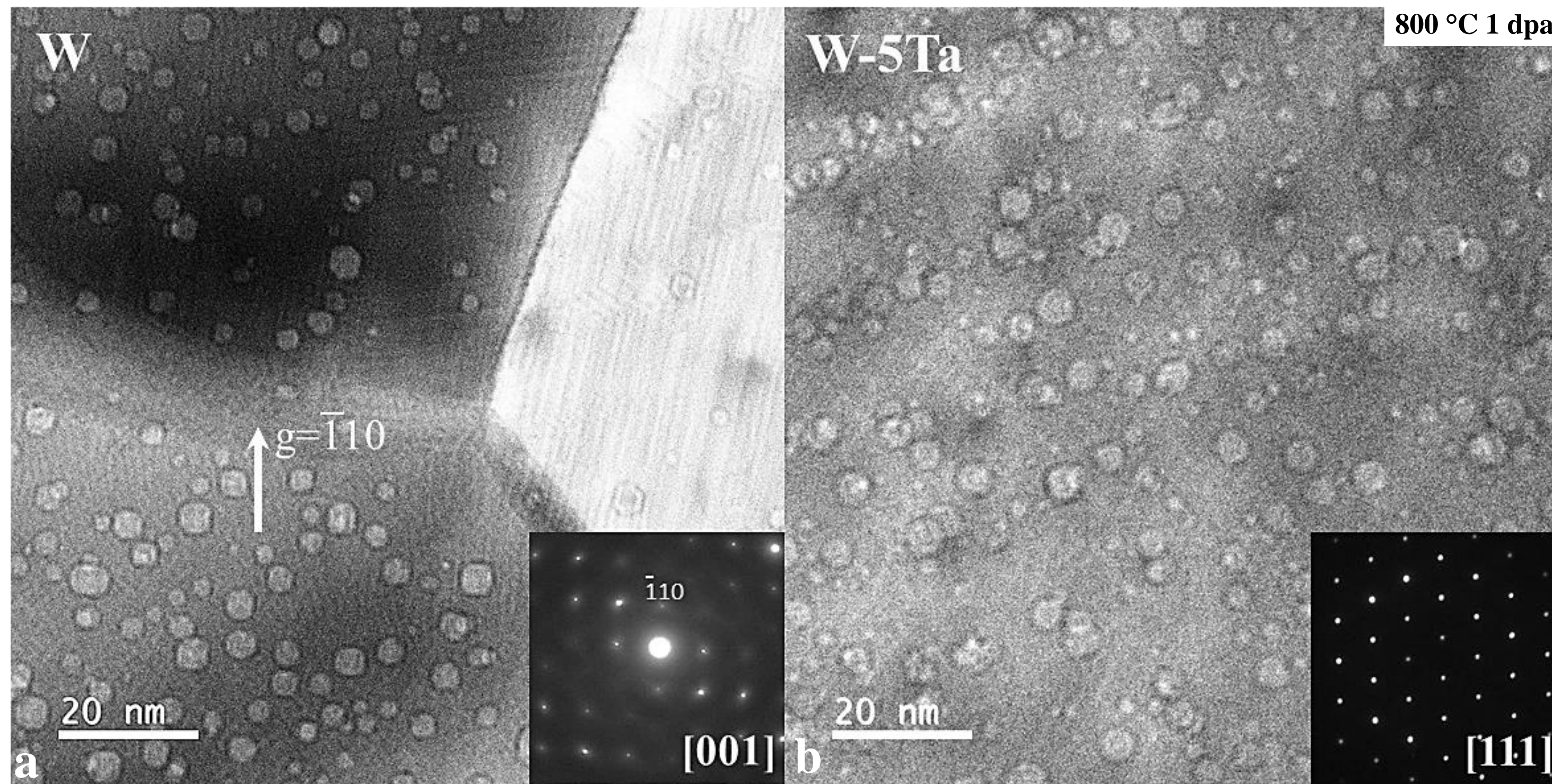


Figure 8

